

1 Direct visualization of solute locations in laboratory ice samples

2
3 Ted Hullar¹, Cort Anastasio¹

4
5 [1] Department of Land, Air, and Water Resources, University of California, Davis

6
7 Correspondence to Cort Anastasio (canastasio@ucdavis.edu)

8 Abstract

9
10 Many important chemical reactions occur in polar snow, where solutes may be present in several
11 reservoirs, including at the air-ice interface and in liquid-like regions within the ice matrix. Some recent
12 laboratory studies suggest chemical reaction rates may differ in these two reservoirs. While
13 investigations have examined where solutes are found in natural snow and ice, few studies have examined
14 solute locations in laboratory samples, nor the possible factors controlling solute segregation. To address
15 this, we used micro-computed tomography (microCT) to examine solute locations in ice samples prepared
16 from either aqueous cesium chloride (CsCl) or Rose Bengal solutions that were frozen using several
17 different methods. Samples frozen in a laboratory freezer had the largest liquid-like inclusions and air
18 bubbles, while samples frozen in a custom freeze chamber had somewhat smaller air bubbles and
19 inclusions; in contrast, samples frozen in liquid nitrogen showed much smaller concentrated inclusions
20 and air bubbles, only slightly larger than the resolution limit of our images (~2 μm). Freezing solutions in
21 plastic versus glass vials had significant impacts on the sample structure, perhaps because the poor heat
22 conductivity of plastic vials changes how heat is removed from the sample as it cools. Similarly, the
23 choice of solute had a significant impact on sample structure, with Rose Bengal solutions yielding smaller
24 inclusions and air bubbles compared to CsCl solutions frozen using the same method. Additional
25 experiments using higher-resolution imaging of an ice sample show that CsCl moves in a thermal
26 gradient, supporting the idea that the solutes in ice are present in mobile liquid-like regions. Our work
27 shows that the structure of laboratory ice samples, including the location of solutes, is sensitive to
28 freezing method, sample container, and solute characteristics, requiring careful experimental design and
29 interpretation of results.

30 31 1. Introduction

32 Snowpacks can be important locations for a variety of chemical reactions, particularly in polar
33 regions (Bartels-Rausch et al., 2014; Domine and Shepson, 2002). Because light can penetrate several
34 10s of cm into the snowpack, photochemical reactions are particularly important (Grannas et al., 2007),
35 including nitrate photolysis forming NO_x (Beine et al., 2002; Chu and Anastasio, 2003; Jacobi et al.,
36 2004), hydrogen peroxide photolysis forming hydroxyl radical (Chu and Anastasio, 2005; Jacobi et al.,
37 2006), and transformation of organics (Dibb and Arsenault, 2002; Sumner and Shepson, 1999).

38 A variety of potential chemical reactants have been identified in snowpacks; concentrations can
39 vary considerably, with typical concentrations on the order of 10 μM in clean Arctic snows (Yang et al.,
40 1996). Impurities can integrate into snow crystals during formation, or be deposited onto the surface of
41 formed crystals. Reactants and products also partition between the snow crystals and the overlying air;
42 the large surface area of the snow crystals provides an extensive environment for reactions to occur. As
43 the snowpack consolidates and snow grains metamorphose, chemical compounds can remain at the

44 surface of the crystals, or become trapped internally at grain boundaries or triple junctions (Bartels-
45 Rausch et al., 2014; Domine et al., 2008; Grannas et al., 2007).

46 There appear to be three reservoirs for impurities in snow: a quasi-liquid layer (QLL) at the ice-
47 air interface; liquid-like regions (LLRs) within the ice (e.g., at grain boundaries); and in the bulk ice
48 matrix, i.e., between frozen water molecules (Barret et al., 2011; Grannas et al., 2007; Jacobi et al.,
49 2004). While the exact location of solutes in snow is not well understood (Bartels-Rausch et al., 2014),
50 the location is important for several reasons. First, chemicals in a surface QLL can be more readily
51 released to the atmosphere compared to impurities segregated into an internal LLR; furthermore, gas-
52 phase oxidants and other species can readily partition from the air onto solutes at the air-ice interface.
53 Second, photon fluxes can vary considerably in various locations within the snowpack (Phillips and
54 Simpson, 2005), although there appear to be only small differences within crystals themselves (McFall
55 and Anastasio, 2016). Third, the rates of reactions of impurities appear to vary with location. For
56 example, photolysis rates of PAHs (polycyclic aromatic hydrocarbons) have been reported to be up to five
57 times faster in surface QLLs compared to in whole ice samples (where PAHs are likely in LLRs) or in
58 aqueous solution (Kahan and Donaldson, 2007, 2010; Ram and Anastasio, 2009). An investigation of
59 reactions in frozen solutions (Kurkova et al., 2011) suggested the QLL and LLR physical reaction
60 environments are substantially different, with QLLs best represented by a 2D cage and LLRs as a 3D
61 cage. This work also found that the cage effect (i.e., the tendency for a compound to be surrounded by
62 solvent molecules, which can impede the ability of a compound to react) at a given temperature was much
63 more pronounced for reactions occurring in QLLs than LLRs, with solutes in QLLs having less mobility
64 compared to solutes in LLRs.

65 Because of the potential reactivity differences between the reservoirs, understanding reaction
66 rates in different reservoirs requires knowing where solutes are located. Solute locations in natural snow
67 and ice samples have been studied using electron microscopy (Barnes et al., 2003; Lomonaco et al., 2009;
68 Rosenthal et al., 2007), and were found to preferentially segregate to grain boundaries and triple
69 junctions. Additional work has evaluated the nature of these compartments, showing that solutes
70 segregate and concentrate in LLRs (Heger et al., 2005; Heger et al., 2006). When an aqueous solution is
71 frozen, most solutes are excluded from the forming ice matrix (Hobbs, 1974; Petrenko and Whitworth,
72 1999), often forming platelets of ice separated by brine or dendritic structures (Rohatgi and Adams, 1967;
73 Shumskii, 1964). Recently, some studies have used various techniques to directly examine the location of
74 solutes themselves in laboratory snow and ice samples (Cheng et al., 2010; Miedaner, 2007; Miedaner et
75 al., 2007) Nonetheless, solute location is poorly understood in many experimental systems, and , is most
76 often inferred from the way the sample is made (Kahan et al., 2010) or from chemical behavior (Kurkova
77 et al., 2011).

78 The main goal of this paper is to examine the location of solutes in laboratory-prepared frozen
79 solutions. In order to do this, we use X-ray computed tomography (CT), a technique that has been used to
80 create 3-dimensional images of a variety of biological and natural materials (Blanke et al., 2013; Evans et
81 al., 2008). High resolution microCT, which is capable of a spatial resolution of $< 10 \mu\text{m}$, has been used to
82 look at the structure of natural snow and ice (Chen and Baker, 2010; Heggli et al., 2011; Lomonaco et al.,
83 2011; Obbard et al., 2009). But to our knowledge this method has not been used to investigate the
84 structure and solute locations for laboratory samples prepared under reproducible conditions with specific
85 solutes.

86 Thus here we examine the locations of impurities in frozen aqueous solutions prepared in the
87 laboratory. We are primarily interested in the locations of solutes in ices prepared using different freezing

88 methods aimed at putting solutes in specific reservoirs within the ice; these methods, or similar ones, have
89 been used both in our previous research as well as by other investigators. In this work we focus on
90 cesium chloride (CsCl) as our solute. However, because previous studies (Cheng et al., 2010; Rohatgi
91 and Adams, 1967) found different solutes can affect freezing morphology and therefore may influence
92 solute location, we also imaged ice containing the organic compound Rose Bengal (4,5,6,7-tetrachloro-
93 2',4',5',7'-tetraiodofluorescein). For our samples we present both qualitative (visual) and semi-
94 quantitative (tabular and graphical) results.

95

96 **2. Methods**

97 We prepared samples by freezing 1.0 mM aqueous solutions of cesium chloride or, in a few
98 cases, 1.0 mM Rose Bengal. High purity water (“Milli-Q water”) was produced from house-treated
99 deionized water that was run through a Barnstead International DO813 activated carbon cartridge and
100 then a Millipore Milli-Q Plus system. We chose cesium chloride (Sigma-Aldrich, 99.9%) for our primary
101 solute because of its high solubility in water and high X-ray mass attenuation coefficient ($\sim 4.4 \text{ cm}^2 \text{ g}^{-1}$ at
102 70 keV (NIST, 2015)), enabling visualization of low concentrations in our microCT system. We also
103 used Rose Bengal to study the impacts of solute size and polarity on sample morphology. While 1.0 mM
104 of solute is higher than typical total solute concentrations in continental (inland) natural snows, it is
105 within the range of concentrations measured in coastal snowpacks (Beine et al., 2011; Douglas and Sturm,
106 2004; Yang et al., 1996). The chosen concentration allows easy visualization in our system and provides
107 enough material to evaluate spatial patterns in the sample.

108 We froze most samples as a 500 μl aliquot in a capped glass vial (approximately 3 cm high and 1
109 cm in diameter, 0.8 mm wall thickness, with a total vial volume of $\sim 2 \text{ ml}$) using one of three methods.
110 These methods were chosen because they had been used in our laboratory, as well as others, and also due
111 to differences in the speed of heat removal from the samples; we discuss later the expected morphologies
112 for the various sample types. In the first technique (“Freezer”), we placed samples upright on a plastic
113 plate in a laboratory freezer at approximately -20°C ; freezing took approximately 1 hour. In the second
114 technique (“Freeze Chamber”), we froze samples upright in a custom-built freeze chamber (Hullar and
115 Anastasio, 2011) whose base was cooled to either -10 or -20°C . Typically, the sample sat directly on the
116 base of the freeze chamber surrounded by air. However, we also froze some samples surrounded by
117 drilled metal plates, effectively placing the sample in a metal “well”; the distance between the sample and
118 the surrounding plates was around 1 mm. In the third technique (“Liquid Nitrogen” or “LN2”) we froze
119 samples by putting the aqueous sample in a vial, capping it, then immersing it in a bath of liquid nitrogen
120 deeper than the height of the liquid in the vial; freezing time was ~ 30 seconds. We allowed all samples to
121 anneal at -10°C for at least 1 hour before imaging. We froze a small number of samples in either
122 polypropylene vials (wall thickness $\sim 1 \text{ mm}$) or with a larger sample volume (750 μl).

123 We imaged samples using a MicroXCT-200 (Zeiss Instruments) micro-computed tomography
124 (microCT) scanner. To maintain our samples at -10°C , samples were held in a custom cold stage for the
125 MicroXCT-200 (Hullar et al., 2014). The custom cold stage was placed on the scanner’s sample stage,
126 whose position is controlled by the scanner software to submicron precision. Scanning parameters were
127 set based on the manufacturer’s guidelines. For most imaging, we set source and detector distances to 40
128 and 130 mm respectively; voltage and power were set at 70 keV and 7.9 W, and the manufacturer’s LE3
129 custom filter was used for beam filtration. The microCT acquired 1600 projections over 360 degrees of
130 rotation, with an exposure time of 2 s. Images were reconstructed using the manufacturer’s software on
131 an isotropic voxel grid with 15.9358 μm edge lengths. Some samples were analyzed at higher resolution,

132 with a voxel edge length of 2.1146 μm . For these samples, we set source and detector distances to 60 and
133 18 mm, used the LE5 beam filter, collected 2400 projections spanning 360 degrees, and set beam voltage,
134 power, and exposure time to 60 keV, 6 W, and 30 s respectively. The microCT scanner software outputs
135 slicewise TIFF images of the X-Y plane of the sample, with greyscale values corresponding to the
136 radiodensity of each voxel at that Z plane.

137 We imported digital TIFF images into the Amira software package (Visualization Sciences
138 Group, FEI) for reconstruction and segmentation. Our segmentation procedure used the Amira
139 segmentation tools to isolate the sample from surrounding materials; generally, our procedure should
140 include very little sample container at the expense of excluding some small amounts of sample in contact
141 with the vial wall. Similarly, the segmentation procedure excludes very little sample in contact with air
142 above the sample, while including small amounts of top air as sample. Some images presented here were
143 mathematically smoothed by the software, which sometimes resulted in small features ($< 80 \mu\text{m}$ in
144 diameter) being eliminated from movies and still images; however, smoothing did not substantially
145 change the interpretation of our results. In some cases we prepared histograms of the data, which were not
146 smoothed and include all sample data.

147 To quantitate CsCl concentration in each voxel, we first imaged samples of Milli-Q water, as both
148 liquid and ice, and measured the average radiodensity (image greyscale value) of a subvolume within
149 each sample. As expected, the average radiodensity of ice ($4948 \pm 160 (1\sigma)$) was less than that of liquid
150 water ($5372 \pm 194 (1\sigma)$) due to the lower density of ice. Our measured radiodensity ratio between ice (at -
151 10°C) and water (at 20°C) was 0.921, matching a calculated density ratio from literature values (Haynes,
152 2014) of 0.921. Next, we imaged 8 aqueous solutions of CsCl at varying concentrations (1.0 mM to 5.0
153 M) to construct a calibration curve. Plotting these points (Fig. 1) shows a linear relationship between
154 CsCl concentration and measured radiodensity, with a y-intercept value within the range of our measured
155 radiodensities for pure liquid water. Therefore, the measured radiodensity of a voxel within a sample
156 containing CsCl in solution (or ice) is linearly related to the amount of CsCl present in the voxel. We
157 assume the relationship between CsCl concentration and radiodensity is the same for ice and water. This
158 allows us to determine the amount of CsCl present in a sample voxel by subtracting the average greyscale
159 value of pure water (or ice) and then using the standard curve to calculate the CsCl mass.

160 When aqueous solutions are frozen, solutes are generally excluded from the forming ice matrix,
161 resulting in a two distinct components: pure (or nearly pure) water ice, and a concentrated solution of
162 solute (Cho et al., 2002; Lake and Lewis, 1970; Wettlaufer et al., 1997), which can be present at the air-
163 ice interface (i.e., as a QLL) and/or in LLRs within the sample. Freezing-point depression dictates that
164 the solute concentration in these regions is solely a function of the ice temperature (Cho et al., 2002) and
165 is independent of the solute concentration in the initial solution. For example, at -10°C , the predicted
166 total solute concentration in LLRs is 5.4 M of solute ions, or 2.7 M of a binary salt such as CsCl. This
167 LLR concentration is considerably lower than the solubility limit of CsCl (11.1 M at 20°C , 9.6 M at 0°C
168 (NIH, 2015)), but higher than the solubility limit of Rose Bengal (1 mM, temperature not given, (Neckers,
169 1989)). Therefore, we do not expect CsCl to precipitate, although Rose Bengal might.

170 As described earlier, we use the Fig. 1 calibration curve to convert microCT greyscale values of
171 radiodensity for each voxel to the mass of solute in each voxel. While this mass could be expressed as an
172 equivalent concentration in the voxel, we believe it is more accurate to consider each voxel as a mixture
173 of pure water ice (with zero solute) and LLRs (regions with a total solute ion concentration of 5.4 M at -
174 10°C , equivalent to a CsCl concentration of 2.7 M). Thus we express the composition of each voxel as
175 the fraction of voxel volume occupied by liquid-like regions, $V_{\text{LLR}}/V_{\text{VOXEL}}$:

176

$$177 \quad \frac{V_{LLR}}{V_{VOXEL}} = \frac{(RD_{MEAS} - RD_{ICE}) / Slope}{2.7 M} \quad (1)$$

178

179 where V_{LLR} is the LLR volume, V_{VOXEL} represents the volume of the entire voxel, RD_{MEAS} is the
180 measured radiodensity of the voxel, RD_{ICE} is the radiodensity of pure ice (4948), and Slope is the
181 measured slope of the standard curve line (10409 M^{-1} ; Fig. 1). A voxel containing only pure ice has
182 $V_{LLR}/V_{VOXEL} = 0$, while a voxel composed entirely of 5.4 M total solute in water has $V_{LLR}/V_{VOXEL} = 1$.
183 Our estimated concentration of total solute ion concentration in LLRs is based on theoretical calculations
184 and assumes ideal behavior from the solution (Cho et al., 2002; Pruppacher and Klett, 2010). However, at
185 higher concentrations, solutions can deviate from ideal behavior. Pruppacher and Klett (Pruppacher and
186 Klett, 2010) and Haynes (Haynes, 2014) both present data for the freezing point depression of CsCl, but
187 only up to a salt concentration of 1.8 M (Pruppacher and Klett) or 1.4 M (Haynes). Extrapolating their
188 data to the concentrations expected in our samples (i.e., at $-10 \text{ }^\circ\text{C}$) suggest the CsCl concentration in
189 LLRs would be somewhere between 3 and 3.2 M, i.e., 10 – 20% higher than our ideal case concentration,
190 but neither source presents freezing point depression data measured at such a high concentration. In the
191 absence of measured information for the actual composition of CsCl solutions under our experimental
192 conditions, we have elected to stay with the theoretical prediction of salt concentration of 2.7 M. If the
193 actual LLR solute concentration is higher (lower) than 2.7 M, the V_{LLR}/V_{VOXEL} values presented here
194 would be lower (higher); we estimate the largest magnitude of this error as approximately 20%. For
195 clarity, we use the measured V_{LLR}/V_{VOXEL} values to segment many of our images into four domains:
196 voxels containing only air (defined as $V_{LLR}/V_{VOXEL} < -3.4\%$), voxels containing ice and little or no solute
197 ($V_{LLR}/V_{VOXEL} = -3.4\%$ to 2%), voxels containing a moderate amount of solute ($V_{LLR}/V_{VOXEL} = 2\%$ - 10%),
198 and voxels containing a substantial amount of solute ($V_{LLR}/V_{VOXEL} > 10\%$). We define an “air” voxel as
199 having a radiodensity less than or equal to the average radiodensity of an imaged air sample, i.e., 3996.
200 As noted above, greyscale values from images of pure materials vary somewhat, meaning a clear
201 distinction between two materials with similar average greyscale values is not possible. We chose to set
202 the cutoff for segmenting LLRs at a greyscale value of 5507, a threshold three standard deviations greater
203 than the average greyscale value for pure ice, which will essentially eliminate the problem of identifying
204 water ice as solute. However, because of this high threshold it is quite likely that solute is present in some
205 voxels characterized as “ice”. On the other hand, voxels defined as having an LLR percentage of 2% or
206 greater almost certainly contain solute. For CsCl-containing samples, we calculated the mass of CsCl
207 present in each domain. Because the statistical distributions of voxels containing only pure water ice and
208 those containing $<2\%$ LLR as well as pure water ice overlapped, we could not determine the mass of
209 CsCl present in the “ice” domain directly. Therefore, we assumed any mass not present in either the LLR
210 2% - 10% or LLR $>10\%$ domains is present in the “ice” domain.

211

212 **3. Results and Discussion**

213 We first present imaging results for samples prepared without added solute (frozen Milli-Q
214 water). Figure 2a shows a reconstructed image of a “pure” ice sample prepared by freezing air-saturated
215 Milli-Q in a glass vial in a laboratory freezer; the full movie, which shows the sample rotating, is in
216 Supplemental Fig. S1. Air bubbles are visible as light grey spheroids, and are generally located towards
217 the center of the sample, away from the vial walls and base. This is likely because the entire outer surface

218 of the vial was cooled and the water apparently froze from the outside inward. Supporting this idea, some
219 of the bubbles appear to elongate along the radial axes of the sample, similar to the bubble elongation
220 seen by Carte (Carte, 1961) in a temperature gradient. The isolation of bubbles within the middle of the
221 sample seems to follow Shumskii's (Shumskii, 1964) model of the formation of the "central nucleus",
222 with impurities (in this case, air bubbles) forced to the center of a freezing water mass.

223 Figure 2b shows a reconstruction of a similar Milli-Q sample, but now where the solution was
224 degassed with helium for 30 minutes before freezing; the full movie is in Supplemental Fig. S2. Because
225 He degassing replaces the more soluble nitrogen and oxygen in the air-saturated solution with less soluble
226 helium, fewer bubbles are present in Fig. 2b. The size of the bubbles, however, is roughly similar in the
227 two figures (approximately 150-300 μm), suggesting bubble size is a function of the freezing method, not
228 of the gas itself.

229 Figure 2c shows a histogram of the number of voxels containing various radiodensities,
230 represented here as the ratio $V_{\text{LLR}}/V_{\text{VOXEL}}$, in the two water ice samples. A ratio of zero represents the
231 average radiometric density for pure water ice, with values slightly greater or less than zero indicating
232 noise in the sample images and reconstruction. Voxels containing only air comprise the smaller, second
233 peak centered at approximately $V_{\text{LLR}}/V_{\text{VOXEL}} = -0.05$, which overlaps with the primary (pure ice) peak.
234 Taking into account that the Y axis (voxel count) is a log scale, the two curves show the volume of gas
235 bubbles is clearly less for the helium degassed treatment. Table 1 shows the estimated volumes of water
236 ice and gas bubbles in the two samples, as determined by our segmentation process (see the Methods
237 section). The gas volume in ice made from air-saturated water is approximately 1.4 %, while the ice
238 made from helium-saturated Milli-Q has approximately half the gas volume. Figures 2a and 2b appear to
239 show a larger difference in gas volume between the two samples, suggesting that many of the small
240 bubbles in the sample imaged in Fig. 2b may have been smoothed away and thus not visible. For a
241 solution in equilibrium with air at 25 C, the mole fraction solubility of air (assuming a composition of
242 20% oxygen and 80% nitrogen) is 1.4×10^{-5} , while the value for helium is 7.0×10^{-6} (Haynes, 2014), i.e.,
243 half the concentration of air in the solution. The expected volume of bubbles in the helium degassed
244 treatment agrees well with the observed volume.

245 Next, we examined the effect of freezing method on both freezing morphology and solute
246 location. The Freezer, Freeze Chamber, and LN2 sample preparation methods are described in the
247 Methods section. Figure 3 shows the results of imaging several combinations of freezing method and
248 solute. We start with an image of the ice made by freezing 1.0 mM CsCl in a laboratory freezer. As
249 shown in Fig. 3a (and the Supplemental Fig. S3 movie), both air bubbles and concentrated CsCl LLRs are
250 relatively large, with the LLRs tending to wrap around the air bubbles. Figure 3b is a magnification of
251 the red-bordered area in Fig. 3a, showing examples of large solute inclusions wrapped around air bubbles
252 (lighter gray spheroids).

253 Figure 3c (movie: Supplemental Fig. S4) shows a similarly prepared sample as the Freezer
254 sample in Fig. 3a, but frozen in our Freeze Chamber. Compared to the Freezer sample, the Freeze
255 Chamber sample has smaller air bubbles and inclusions, more solute present near the top of the sample,
256 and the areas of concentrated solutes (LLRs) are less likely to be associated with the air bubbles. These
257 points are clearly shown in Fig. 3d, which is a magnification of the red bordered area of Fig. 3c.
258 Considering that these two samples were frozen at similar temperatures, the morphologies are
259 substantially different. As seen in Table 1, the fraction of voxels containing a LLR fraction $>10\%$ is
260 about five-fold less in the Freeze Chamber sample than the Freezer sample, while the fraction of voxels
261 with an LLR concentration between 2 and 10% doubles. This finding indicates the freezing process in the

262 freeze chamber creates smaller LLR inclusions than does the freezer, with LLRs distributed more widely
263 throughout the sample. Additionally, substantial amounts of solute were segregated towards the surface
264 of the Freeze Chamber sample; presumably, the sample froze from the bottom and solutes were
265 preferentially excluded from the advancing freezing front. However, the same process did not affect the
266 air bubbles, which are well distributed throughout the sample. We believe these structural differences may
267 be due to faster freezing in the Freeze Chamber sample, as the freeze chamber removes heat more quickly
268 than the freezer because of direct contact between the bottom of the vial and the chilled base plate in the
269 chamber. Previous work (Hallett, 1964; Rohatgi and Adams, 1967) has shown faster freezing gives closer
270 spacing of ice dendrites or plates in the sample as it freezes, which then leads to smaller solute inclusions
271 or bubbles, similar to our finding here. Supplemental Fig. S5 shows a sample prepared in the same way
272 as in Fig. 3c, but with the metal plates in place in the freeze chamber, which surrounds the vial with metal
273 rather than air. Here, we see similar bubble size and location as the sample frozen in the freeze chamber
274 without the metal plates. However, unlike the sample frozen without plates in the freeze chamber, the
275 solute distribution with plates shows no segregation towards the top of the sample, probably because the
276 close proximity of the conductive metal plates removed heat from the sides and bottom of the sample
277 simultaneously, similar to the Freezer case.

278 Results for a 1.0 mM CsCl sample prepared with the third freezing method – liquid nitrogen – are
279 shown in Fig. 3e, with the full movie in Supplemental Fig. S6. No air bubbles or significant solute
280 inclusions are visible. However, as discussed earlier, some very small inclusions and air bubbles can be
281 removed by the mathematical smoothing done by the reconstruction software, so very small features (<
282 ~80 μm) may be present in the sample but lost in the reconstruction. A histogram of raw (i.e., not
283 smoothed) greyscale values from the LN2 sample image does show some voxels contain concentrated
284 solutes (Fig. 3g), as indicated by $V_{\text{LLR}}/V_{\text{VOXEL}}$ for some voxels towards the right-hand side of the graph
285 being greater than that of pure water ice. As a further test of the possibility of solute inclusions in LN2
286 samples, we examined unreconstructed cross-sections of a 1.0 mM CsCl sample frozen in liquid nitrogen
287 and imaged at ~2 μm voxel resolution. As illustrated in Supplemental Fig. S7, there are some light
288 (concentrated solute) and dark (air bubble) areas, suggesting some segregation of CsCl and air occurs
289 even with rapid freezing (~30 seconds). However, this effect is less noticeable in the quickly frozen
290 liquid nitrogen sample (Supplemental Fig. S7), and much more pronounced in the other two freezing
291 methods (Figs. 3a and 3c). Analogous findings, although using a very different experimental system,
292 were reported by Heger et al. (Heger et al., 2005), who found solutes were concentrated by as many as six
293 orders of magnitude with slow (several minutes) freezing, but only three orders of magnitude when frozen
294 in liquid nitrogen.

295 Figure 3g shows the histogram for the 1.0 mM CsCl solutions frozen using each of the three
296 freezing methods, as well as for Milli-Q water ice frozen in a laboratory freezer. Unlike the images seen
297 in Figs. 3a through 3f, where mathematical smoothing can eliminate small structures, the histograms
298 include all the voxels in the sample. As discussed in Fig 2c, water ice has two overlapping peaks,
299 corresponding to air bubbles (left peak) and ice (right peak). Some voxels, shown in the “saddle”
300 between the two peaks, contain both air bubbles and pure water ice, and will therefore have a greyscale
301 value between air and ice. The Fig. 3g histogram clearly shows how CsCl tends to be present in larger
302 LLR volumes in the Freezer sample, including some voxels that are almost completely composed of 2.7
303 M CsCl solution, with a maximum $V_{\text{LLR}}/V_{\text{VOXEL}}$ of 0.9. This finding supports the idea of solutes
304 segregating to concentrated LLRs during freezing, since if solutes were precipitating and forming solid
305 inclusions in the bulk ice, the calculated ratio in a voxel could be higher than 1. The fact that the ratio

306 gets close to, but never exceeds, 1 is consistent with our tricomponent model of air, relatively pure ice,
307 and concentrated LLRs with a maximum concentration of 5.4 M total solute.

308 The increased number of air voxels on the left end of the curve for the 1.0 mM CsCl freezer
309 sample represents voxels composed entirely of air. This number is larger than in the water sample,
310 supporting the imaging findings that the presence of solute actually increases the size of air bubbles. For
311 the Freeze Chamber and LN2 samples, the number of voxels containing only air is smaller, and voxels
312 containing air are more likely to contain at least some fraction of ice or solute. For the Freeze Chamber
313 sample, the histogram correlates with the images (2c and 2d), with fewer voxels containing a large
314 volume fraction of highly concentrated regions than in the Freezer sample. Finally, the liquid nitrogen
315 histogram is nearly identical to water ice, although a few voxels with concentrated solute are present (also
316 seen in Supplemental Fig. S7). Next, we examined the impact of solute on freezing morphology and
317 solute location, by replacing CsCl with Rose Bengal, a large, organic molecule (see structure in
318 Supplemental Fig. S8). Figure 3f (movie: Supplemental Fig. S9) shows a sample containing 1.0 mM
319 Rose Bengal frozen in our freeze chamber. Using 1.0 mM Rose Bengal instead of 1.0 mM CsCl (Fig. 3c)
320 gives a very different freezing pattern, with only a few small bubbles and no visible areas of concentrated
321 solute. While mathematical smoothing has likely eliminated some of the smaller structures, the overall
322 sample morphology is quite different than that produced by the same concentration of CsCl. Miedaner
323 and Miedaner and co-workers (Miedaner, 2007; Miedaner et al., 2007), using different compounds, also
324 found that sample morphology was highly sensitive to solute identity. Interestingly, changing solute in
325 our system alters not only the structure of solute inclusions, but also the size of the air bubbles. The exact
326 reason for the change in morphology is unclear. CsCl is more polar than Rose Bengal, and could
327 influence the movement of the polar water molecules into the forming ice matrix. As a relatively large
328 organic molecule, Rose Bengal might potentially modify the ice matrix due to its size. Finally, we note
329 the thermodynamically predicted final concentration of solute ions at -10°C is 5.4 M; at this
330 concentration CsCl should still be in solution, while a substantial portion of the Rose Bengal should have
331 precipitated. Whether precipitated Rose Bengal is present as solids incorporated into the ice matrix or as
332 precipitates in LLRs is not known.

333 The reproducibility of samples prepared on different days but using identical methods was quite
334 good, with similar patterns seen for each replicate (Supplemental Fig. S10). Each combination of
335 freezing method and solute gave a distinct distribution of solute and air bubbles, suggesting these two
336 variables have a significant impact on ice morphology in our experimental system.

337 Table 1 lists the calculated volume of each material domain and the total CsCl mass present,
338 including all sample voxels, based on segmentation described in the Methods section. As seen in the
339 images and histogram, the Freezer sample has the highest fraction (0.00019) of voxels containing 10% or
340 more LLR volume, approximately 5 times greater than the Freeze Chamber sample. In contrast, the
341 fraction of voxels with $V_{\text{LLR}}/V_{\text{VOXEL}} = 2\text{-}10\%$ in the Freezer sample (0.003) is about half that in the Freeze
342 Chamber sample, and the fraction of gas bubbles appears to be less than in the Freeze Chamber sample.
343 However, this may be a computational artifact; voxels containing LLR next to gas bubbles will have a
344 greyscale value somewhere between air and LLR, and therefore may be mistakenly counted as water ice
345 voxels. Unfortunately, determining the magnitude of this error is difficult -requiring estimating the
346 surface area of both air bubbles and any adjacent LLRs to identify suspect voxels - and is beyond the
347 scope of this study. Because LLRs in the Freezer samples are more concentrated and appear to be more
348 frequently found next to air bubbles (as seen in Fig. 3b), this effect may be more pronounced in the
349 Freezer samples than Freeze Chamber samples. However, the number of voxels mistakenly classified as

350 water (or less concentrated solute) is limited to boundaries between air and LLRs and therefore small, and
351 should not affect the overall interpretation of results. Examining the location of the CsCl mass, more than
352 10% of all CsCl present in the Freezer sample is found in voxels with LLRs >10%, while in the Freeze
353 Chamber sample only around 1% of the mass is found in these most concentrated LLRs. For both Freezer
354 and Freeze Chamber samples, about two-thirds of the CsCl mass is found in the ice compartment,
355 suggesting most solutes are present in very small LLR inclusions that are indistinguishable from water
356 ice. For the LN2 sample, only 12% of the mass is found in detectable LLRs, with the remainder
357 distributed throughout the water ice. It is also possible that the CsCl in the LN2 samples is present not as
358 liquid inclusions, but as solid solution within the water ice. However, the solubility of HCl in solid ice is
359 $(1-2) \times 10^{-4}$ M (Gross et al., 1975), while the CsCl solubility in solid ice would need to be 5-10 times
360 greater, assuming all the CsCl is present in solid solution. The “missing” CsCl mass here is $0.88 * 126.3$
361 $\mu\text{g} = 111.1 \mu\text{g}$, or $0.66 \mu\text{mol}$. Assuming this solute is entirely present as LLRs with solute concentration
362 of 2.7 M, this equates to a total LLR volume of $0.24 \mu\text{L}$. The volume of pure ice (again from Table 1) is
363 $725 \mu\text{L}$. Therefore, assuming the remaining CsCl is distributed equally throughout the voxels labeled as
364 pure ice in Table 1, the calculated average $V_{\text{LLR}}/V_{\text{VOXEL}}$ for these voxels is 0.034%, indistinguishable
365 from water ice in our system. While it is possible the CsCl is present (at least partially) as solutes in the
366 solid ice matrix, we believe it is more likely to be present primarily as small LLR inclusions.
367 Additionally, we present evidence later in this paper supporting the idea that solutes are predominantly
368 present as LLR inclusions.

369 We next examined the impact of sample container on sample morphology and solute distribution
370 by imaging samples frozen in plastic vials instead of the glass vials we used above. While many of the
371 samples discussed thus far were frozen in the laboratory freezer, most of the samples prepared in plastic
372 vials were frozen in the freeze chamber. Therefore, to allow appropriate comparisons, we first present a
373 sample of water (no solute) frozen in the freeze chamber and compare this with previous samples frozen
374 in the freezer. Milli-Q water frozen in the freeze chamber in a glass vial (Supplemental Fig. S11) gives
375 similar spatial distribution and somewhat smaller air bubbles sizes as a similar sample frozen in a
376 laboratory freezer (Fig. 2a and Supplemental Fig. S1). However, freezing water in a plastic vial rather
377 than glass can make a significant difference in ice morphology, as shown in Supplemental Fig. S12.
378 While ice in a glass vial forms many roughly spherical bubbles, water frozen in a plastic vial using our
379 freeze chamber forms long vertical channels; such directional growth of air bubbles in a freezing liquid
380 has previously been reported (Carte, 1961). While the reason for this morphology is not entirely clear, ,
381 we believe it is related to how heat is removed from the sample during freezing. Because plastic
382 conducts heat more poorly than water, ice, or glass, the vial walls act as insulators, forcing heat to be
383 primarily removed from the bottom of the sample where the plastic vial contacts the chilled plate at the
384 base of the freeze chamber. This may promote the formation of vertical air channels as the ice freezes
385 upwards through the sample, rather than from the walls towards the interior in the glass vial sample.

386 We next examine the impact of freezing in plastic for a sample containing solutes. Supplemental
387 Fig. S13 shows a 1.0 mM CsCl solution frozen in the freezer in a plastic vial; compared to the similarly
388 treated sample frozen in a glass vial (Fig. 3a), the air bubbles and concentrated inclusions are smaller in
389 the plastic vial. Interestingly, the air bubbles in the plastic vial CsCl Freezer sample do not show any of
390 the elongation found when Milli-Q water is frozen in a plastic vial in the freeze chamber (Supplemental
391 Fig. S12), which may be related to the directional heat removal in the freeze chamber. Finally, once again
392 using the freeze chamber, Supplemental Fig. S14 shows 1.0 mM Rose Bengal frozen in plastic in the

393 freeze chamber. Here, we see substantial volumes of LLRs and more bubbles than seen in the sample
394 frozen in a glass vial, but without any elongation to bubbles or LLRs.

395 We also performed several other experiments to examine the nature of LLRs. Figure 4 shows a
396 cross-section of microCT images of the same sample (1.0 mM CsCl, frozen in freezer) at voxel
397 resolutions of 16 μm (left) and 2 μm (right); the corresponding movies are in Supplemental Fig. S15. The
398 areas of light grey in the lower resolution image (16 μm voxel resolution), such as the area highlighted by
399 the arrow, are likely areas where CsCl is present in small areas of concentrated LLRs bordered by pure
400 water ice, although the voxel resolution does not show these features separately. As would be expected if
401 freezing water effectively excludes solutes from the forming bulk ice matrix, the right hand image shows
402 areas of concentrated LLRs adjacent to areas of pure water ice, supporting the idea discussed earlier that
403 during freezing solutes are preferentially excluded from the forming ice matrix into small areas of
404 concentrated solution. The higher resolution image in Fig. 4 also shows very clearly how the solutes in
405 LLRs often wrap around the bubbles in the Freezer CsCl samples.

406 Finally, Fig. 5 (and the accompanying movie in Supplemental Fig. S16) further supports the idea that
407 CsCl is contained in liquid-like regions in our ice samples. We placed a 1.0 mM CsCl sample (glass vial;
408 Freezer) in the microCT sample holder set at $-10\text{ }^{\circ}\text{C}$ and took images of the sample (2 μm voxel
409 resolution, X-Z plane) at 0, 11, and 22 hours. The temperature gradient in the sample holder was
410 measured later by placing a thermocouple sensor between the glass vial and the holder wall at various
411 positions. The temperature difference between the bottom and middle of the holder (approximately 1.7
412 cm, extending above and below the 1 cm height of the frozen sample in the vial) was $2.2\text{ }^{\circ}\text{C}$, resulting in a
413 temperature gradient of $0.13\text{ }^{\circ}\text{C mm}^{-1}$. As seen in the three images, over the 22 hours of this experiment
414 the bright areas of CsCl move in the direction of the temperature gradient, towards the warmer top of the
415 vial, at a rate of approximately $10\text{ }\mu\text{m h}^{-1}$. (i.e., $7.7\text{ }\mu\text{m h}^{-1}/(\text{K}^{-1}\text{ cm}^{-1})$). In many cases, the solutes appear
416 to be migrating around the surfaces of air bubbles, which are visible as darker grey spheres. While the air
417 bubbles appear to remain stationary in the ice matrix, with an estimated maximum migration rate of 0.15
418 $\mu\text{m h}^{-1}/(\text{K}^{-1}\text{ cm}^{-1})$, the CsCl moves. Solute is excluded from the forming ice matrix during freezing
419 (Hobbs, 1974; Petrenko and Whitworth, 1999); here, it appears the solutes are present as a concentrated
420 liquid-like solution, which can migrate either along the boundaries between air bubbles and the bulk ice,
421 or possibly by melting into the bulk ice itself (Notz and Worster, 2009). While we cannot rule out the
422 possibility that the migrating solutes might be present as solid salt crystals, as seen in other work for ice
423 under a temperature gradient (Light et al., 2009), the moving solutes in our images appear to be in liquid-
424 like regions. Previous studies have found bubbles migrate in a temperature gradient at rates of around
425 $1.5\text{-}3\text{ }\mu\text{m h}^{-1}/(\text{K}^{-1}\text{ cm}^{-1})$ (Dadic et al., 2010), while brine inclusions move at around $10\text{ }\mu\text{m h}^{-1}/(\text{K}^{-1}\text{ cm}^{-1})$
426 (Light et al., 2009). While our results support the idea of brine moving faster than bubbles, the relative
427 rates in our experiments seem much different (with the bubbles moving slower and the brine moving
428 faster) than suggested by previous literature. However, the earlier studies were done in systems
429 containing either bubbles or brine inclusions, not both; as noted by Light (Light et al., 2009), “The effect
430 of included gas bubbles on brine migration has not been studied.”

431

432 **4. Implications and Conclusions**

433 Using microCT we directly visualized the locations of solute, gas, and bulk ice in laboratory-
434 prepared ice samples. While the chemical concentrations we used are higher than those in clean polar
435 samples, because of the substantial morphological differences seen between pure ice samples and solute-
436 containing samples, we expect that solutes in natural snow and ice might sometimes have important
437 impacts on sample morphology, including the location and sizes of liquid-like regions and air bubbles.

438 Highlighting the sensitivity of ice structure to freezing conditions, we found a large difference
439 between samples prepared at freezing temperatures in an upright freezer (where the sample was
440 surrounded by cold air) versus our custom-built freeze chamber (where the sample sat on a cold plate).
441 Samples frozen in liquid nitrogen, as expected, did not have the large air bubbles and LLR inclusions
442 found in Freezer or Freeze Chamber samples; nonetheless, we did find some evidence for the segregation
443 of solutes into LLRs, even with the fast freezing of liquid nitrogen.

444 In addition to freezing conditions, the choice of solute (either Cesium chloride or Rose Bengal)
445 also impacted the ice sample structure differently; CsCl yielded larger air bubbles and solute inclusions
446 compared to Rose Bengal. While the observed variations in the locations and sizes of solute inclusions
447 might be expected for solutes of different polarity and size, the influence of solute on bubble morphology
448 is more surprising. CsCl samples frozen in our laboratory freezer showed large LLRs, often wrapping
449 around air bubbles. While QLLs at the surface ice-air interface of ice or snow are obviously in contact
450 with atmospheric oxidants, the preferential collocation of internal LLRs and air bubbles represents a
451 previously unrecognized air-ice interface. Depending on the chemistry occurring at this interface, the
452 bubbles might be a source of oxidants and other gas-phase chemicals to internal solutes, and might have
453 significant impacts for chemical transformations under certain conditions.

454 Our results here suggest that subtle changes in the preparation of laboratory ice samples can have
455 significant impacts on the location of solutes in samples, requiring careful and consistent sample
456 preparation to ensure meaningful results. Ideally, researchers would directly evaluate the location of
457 solutes for each sample preparation method, as we have done here; we recognize, however, this is a
458 significant undertaking and not possible for every laboratory to do. Beyond the impacts on laboratory
459 science, our work here may be able to help guide further investigations to understand the driving forces
460 shaping snow and ice structures in the natural world, as well as investigations of the rate of chemical
461 reactions in various compartments in snow and ice.

462

463 **Supplemental Information**

464 Supplemental information is available at <http://dx.doi.org/10.1594/PANGAEA.855461>.

465

466 **Acknowledgements**

467 We gratefully acknowledge thorough and insightful comments from Hans-Werner Jacobi, Sönke Maus,
468 and one anonymous reviewer. We thank Doug Rowland for microCT imaging assistance, David Paige
469 (Paige Instruments) for constructing the temperature-controlled microCT sample chamber, and Bill
470 Simpson and Peter Peterson for useful conversations and suggestions. We are grateful for funding from
471 the National Science Foundation (grant CHE-1214121).

472

473 **References**

- 474
475 Barnes, P. R. F., Wolff, E. W., Mallard, D. C., and Mader, H. M.: SEM studies of the morphology and
476 chemistry of polar ice, *Microsc Res Tech*, 62, 62-69, 10.1002/jemt.10385, 2003.
477
478 Barret, M., Domine, F., Houdier, S., Gallet, J. C., Weibring, P., Walega, J., Fried, A., and Richter, D.:
479 Formaldehyde in the Alaskan Arctic snowpack: Partitioning and physical processes involved in air-snow
480 exchanges, *J Geophys Res-Atmos*, 116, 10.1029/2011jd016038, 2011.
481
482 Bartels-Rausch, T., Jacobi, H. W., Kahan, T. F., Thomas, J. L., Thomson, E. S., Abbatt, J. P. D.,
483 Ammann, M., Blackford, J. R., Bluhm, H., Boxe, C., Domine, F., Frey, M. M., Gladich, I., Guzman, M.
484 I., Heger, D., Huthwelker, T., Klan, P., Kuhs, W. F., Kuo, M. H., Maus, S., Moussa, S. G., McNeill, V.
485 F., Newberg, J. T., Pettersson, J. B. C., Roeselova, M., and Sodeau, J. R.: A review of air-ice chemical
486 and physical interactions (AICD): liquids, quasi-liquids, and solids in snow, *Atmos Chem Phys*, 14, 1587-
487 1633, 10.5194/acp-14-1587-2014, 2014.
488
489 Beine, H., Anastasio, C., Esposito, G., Patten, K., Wilkening, E., Domine, F., Voisin, D., Barret, M.,
490 Houdier, S., and Hall, S.: Soluble, light-absorbing species in snow at Barrow, Alaska, *J Geophys Res-*
491 *Atmos*, 116, 10.1029/2011jd016181, 2011.
492
493 Beine, H. J., Domine, F., Simpson, W., Honrath, R. E., Sparapani, R., Zhou, X. L., and King, M.: Snow-
494 pile and chamber experiments during the Polar Sunrise Experiment 'Alert 2000': exploration of nitrogen
495 chemistry, *Atmos Environ*, 36, 2707-2719, 10.1016/s1352-2310(02)00120-6, 2002.
496
497 Blanke, A., Beckmann, F., and Misof, B.: The head anatomy of *Epiophlebia superstes* (Odonata:
498 *Epiophlebiidae*), *Org Divers Evol*, 13, 55-66, 10.1007/s13127-012-0097-z, 2013.
499
500 Carte, A. E.: Air bubbles in ice, *Proceedings of the Physical Society of London*, 77, 757-&
501 10.1088/0370-1328/77/3/327, 1961.
502
503 Chen, S., and Baker, I.: Evolution of individual snowflakes during metamorphism, *J Geophys Res-Atmos*,
504 115, 10.1029/2010jd014132, 2010.
505
506 Cheng, J., Soetjijto, C., Hoffmann, M. R., and Colussi, A. J.: Confocal Fluorescence Microscopy of the
507 Morphology and Composition of Interstitial Fluids in Freezing Electrolyte Solutions, *J Phys Chem Lett*,
508 1, 374-378, 10.1021/jz9000888, 2010.
509
510 Cho, H., Shepson, P. B., Barrie, L. A., Cowin, J. P., and Zaveri, R.: NMR investigation of the quasi-brine
511 layer in ice/brine mixtures, *J Phys Chem B*, 106, 11226-11232, 10.1021/jp020449+, 2002.
512
513 Chu, L., and Anastasio, C.: Quantum yields of hydroxyl radical and nitrogen dioxide from the photolysis
514 of nitrate on ice, *J Phys Chem A*, 107, 9594-9602, 10.1021/jp0349132, 2003.
515
516 Chu, L., and Anastasio, C.: Formation of hydroxyl radical from the photolysis of frozen hydrogen
517 peroxide, *J Phys Chem A*, 109, 6264-6271, 10.1021/jp051415f, 2005.
518
519 Dadic, R., Light, B., and Warren, S. G.: Migration of air bubbles in ice under a temperature gradient, with
520 application to "Snowball Earth", *J Geophys Res-Atmos*, 115, 8, 10.1029/2010jd014148, 2010.
521

522 Dibb, J. E., and Arsenault, M.: Shouldn't snowpacks be sources of monocarboxylic acids?, *Atmos*
523 *Environ*, 36, 2513-2522, 2002.

524

525 Domine, F., and Shepson, P. B.: Air-snow interactions and atmospheric chemistry, *Science*, 297, 1506-
526 1510, 2002.

527

528 Domine, F., Albert, M., Huthwelker, T., Jacobi, H. W., Kokhanovsky, A. A., Lehning, M., Picard, G., and
529 Simpson, W. R.: Snow physics as relevant to snow photochemistry, *Atmos Chem Phys*, 8, 171-208, 2008.

530

531 Douglas, T. A., and Sturm, M.: Arctic haze, mercury and the chemical composition of snow across
532 northwestern Alaska, *Atmos Environ*, 38, 805-820, 10.1016/j.atmosenv.2003.10.042, 2004.

533

534 Evans, N. J., McInnes, B. I. A., Squelch, A. P., Austin, P. J., McDonald, B. J., and Wu, Q. H.:
535 Application of X-ray micro-computed tomography in (U-Th)/He thermochronology, *Chem Geol*, 257,
536 101-113, 10.1016/j.chemgeo.2008.08.021, 2008.

537

538 Grannas, A. M., Jones, A. E., Dibb, J., Ammann, M., Anastasio, C., Beine, H. J., Bergin, M., Bottenheim,
539 J., Boxe, C. S., Carver, G., Chen, G., Crawford, J. H., Domine, F., Frey, M. M., Guzman, M. I., Heard, D.
540 E., Helmig, D., Hoffmann, M. R., Honrath, R. E., Huey, L. G., Hutterli, M., Jacobi, H. W., Klan, P.,
541 Lefer, B., McConnell, J., Plane, J., Sander, R., Savarino, J., Shepson, P. B., Simpson, W. R., Sodeau, J.
542 R., von Glasow, R., Weller, R., Wolff, E. W., and Zhu, T.: An overview of snow photochemistry:
543 evidence, mechanisms and impacts, *Atmos Chem Phys*, 7, 4329-4373, 2007.

544

545 Gross, G. W., Wu, C. H., Bryant, L., and McKee, C.: Concentration dependent solute redistribution at ice-
546 water phase boundary. .2. Experimental investigation, *J Chem Phys*, 62, 3085-3092, 10.1063/1.430909,
547 1975.

548

549 Hallett, J.: Experimental studies of the crystallization of supercooled water, *J Atmos Sci*, 21, 671-682,
550 10.1175/1520-0469(1964)021<0671:esotco>2.0.co;2, 1964.

551

552 Haynes, W. M. e.: *CRC Handbook of Chemistry and Physics*, 95 ed., CRC Press, 2014.

553

554 Heger, D., Jirkovsky, J., and Klan, P.: Aggregation of methylene blue in frozen aqueous solutions studied
555 by absorption spectroscopy, *J Phys Chem A*, 109, 6702-6709, 10.1021/jp050439j, 2005.

556

557 Heger, D., Klanova, J., and Klan, P.: Enhanced protonation of cresol red in acidic aqueous solutions
558 caused by freezing, *J Phys Chem B*, 110, 1277-1287, 10.1021/jp0553683, 2006.

559

560 Heggli, M., Kochle, B., Matzl, M., Pinzer, B. R., Riche, F., Steiner, S., Steinfeld, D., and Schneebeli, M.:
561 Measuring snow in 3-D using X-ray tomography: assessment of visualization techniques, *Ann Glaciol*,
562 52, 231-236, 2011.

563

564 Hobbs, P. V.: *Ice Physics*, Oxford University Press, Oxford, England, 1974.

565

566 Hullar, T., and Anastasio, C.: Yields of hydrogen peroxide from the reaction of hydroxyl radical with
567 organic compounds in solution and ice, *Atmos Chem Phys*, 11, 7209-7222, 10.5194/acp-11-7209-2011,
568 2011.

569

570 Hullar, T., Paige, D. F., Rowland, D. J., and Anastasio, C.: Compact cold stage for micro-computerized
571 tomography imaging of chilled or frozen samples, *Rev Sci Instrum*, 85, 10.1063/1.4871473, 2014.

572
573 Jacobi, H. W., Bales, R. C., Honrath, R. E., Peterson, M. C., Dibb, J. E., Swanson, A. L., and Albert, M.
574 R.: Reactive trace gases measured in the interstitial air of surface snow at Summit, Greenland, *Atmos*
575 *Environ*, 38, 1687-1697, 10.1016/j.atmosenv.2004.01.004, 2004.
576
577 Jacobi, H. W., Annor, T., and Quansah, E.: Investigation of the photochemical decomposition of nitrate,
578 hydrogen peroxide, and formaldehyde in artificial snow, *J Photochem Photobiol A-Chem*, 179, 330-338,
579 10.1016/j.jphotochem.2005.09.001, 2006.
580
581 Kahan, T. F., and Donaldson, D. J.: Photolysis of polycyclic aromatic hydrocarbons on water and ice
582 surfaces, *J Phys Chem A*, 111, 1277-1285, 10.1021/jp066660t, 2007.
583
584 Kahan, T. F., and Donaldson, D. J.: Benzene photolysis on ice: Implications for the fate of organic
585 contaminants in the winter, *Environ Sci Technol*, 44, 3819-3824, 10.1021/es100448h, 2010.
586
587 Kahan, T. F., Zhao, R., Jumaa, K. B., and Donaldson, D. J.: Anthracene photolysis in aqueous solution
588 and ice: Photon flux dependence and comparison of kinetics in bulk ice and at the air-ice interface,
589 *Environ Sci Technol*, 44, 1302-1306, 10.1021/es9031612, 2010.
590
591 Kurkova, R., Ray, D., Nachtigallova, D., and Klan, P.: Chemistry of small organic molecules on snow
592 grains: The applicability of artificial snow for environmental studies, *Environ Sci Technol*, 45, 3430-
593 3436, 10.1021/es104095g, 2011.
594
595 Lake, R. A., and Lewis, E. L.: Salt rejection by sea ice during growth, *J Geophys Res*, 75, 583-&,
596 10.1029/JC075i003p00583, 1970.
597
598 Light, B., Brandt, R. E., and Warren, S. G.: Hydrohalite in cold sea ice: Laboratory observations of single
599 crystals, surface accumulations, and migration rates under a temperature gradient, with application to
600 "Snowball Earth", *J Geophys Res-Oceans*, 114, 17, 10.1029/2008jc005211, 2009.
601
602 Lomonaco, R., Albert, M., and Baker, I.: Microstructural evolution of fine-grained layers through the firn
603 column at Summit, Greenland, *J Glaciol*, 57, 755-762, 2011.
604
605 Lomonaco, R. W., Chen, S., and Baker, I.: Characterization of porous snow with SEM and Micro CT,
606 *Microsc microanal*, 15, 1110-1111, 10.1017/s1431927609093313, 2009.
607
608 McFall, A. S., and Anastasio, C.: Photon flux dependence on solute environment in water ices,
609 *Environmental Chemistry*, <http://dx.doi.org/10.1071/EN15199>, 2016.
610
611 Miedaner, M.: Characterization of inclusions and their distribution in natural and artificial ice samples by
612 synchrotron cryo-micro-tomography (SCXRTM), thesis, 2007.
613
614 Miedaner, M. M., Huthwelker, T., Enzmann, F., Kersten, M., Stampanoni, M., and Ammann, M.: X-ray
615 tomographic characterization of impurities in polycrystalline ice, *Physics and Chemistry of Ice*, edited by:
616 Kuhs, W. F., Royal Soc Chemistry, Cambridge, 399-407 pp., 2007.
617
618 Neckers, D. C.: Rose Bengal, *J Photochem Photobiol A-Chem*, 47, 1-29, 10.1016/1010-6030(89)85002-6,
619 1989.
620
621 NIH: PubChem Open Chemistry Database: <http://pubchem.ncbi.nlm.nih.gov>, access: 7 July 2015, 2015.

622
623 NIST: X-ray form factor, attenuation, and scattering tables:
624 <http://physics.nist.gov/PhysRefData/FFast/html/form.html>, access: 5 July 2015, 2015.
625
626 Notz, D., and Worster, M. G.: Desalination processes of sea ice revisited, *J Geophys Res-Oceans*, 114, 10,
627 10.1029/2008jc004885, 2009.
628
629 Obbard, R. W., Troderman, G., and Baker, I.: Imaging brine and air inclusions in sea ice using micro-X-
630 ray computed tomography, *J Glaciol*, 55, 1113-1115, 2009.
631
632 Petrenko, V. F., and Whitworth, R. W.: *Physics of Ice*, Oxford University Press, Oxford, England, 1999.
633
634 Phillips, G. J., and Simpson, W. R.: Verification of snowpack radiation transfer models using
635 actinometry, *J Geophys Res-Atmos*, 110, D08306 10.1029/2004jd005552, 2005.
636
637 Pruppacher, H. R., and Klett, J. D.: *Microphysics of clouds and precipitation*, Vol. 18 of Atmospheric and
638 oceanographic sciences library, Kluwer Academic
639 Publ., 2010.
640
641 Ram, K., and Anastasio, C.: Photochemistry of phenanthrene, pyrene, and fluoranthene in ice and snow,
642 *Atmos Environ*, 43, 2252-2259, 10.1016/j.atmosenv.2009.01.044, 2009.
643
644 Rohatgi, P., and Adams, C.: Ice-brine dendritic aggregate formed on freezing of
645 aqueous solutions., *J Glaciol* 6, 663-679, 1967.
646
647 Rosenthal, W., Saleta, J., and Dozier, J.: Scanning electron microscopy of impurity structures in snow,
648 *Cold Reg Sci Tech*, 47, 80-89, 10.1016/j.coldregions.2006.08.006, 2007.
649
650 Shumskii, P. A.: *Principles of Structural Glaciology*, Dover Publications, Inc. , New York, USA, 1964.
651
652 Sumner, A. L., and Shepson, P. B.: Snowpack production of formaldehyde and its effect on the Arctic
653 troposphere, *Nature*, 398, 230-233, 1999.
654
655 Wettlaufer, J. S., Worster, M. G., and Huppert, H. E.: Natural convection during solidification of an alloy
656 from above with application to the evolution of sea ice, *Journal of Fluid Mechanics*, 344, 291-316,
657 10.1017/s0022112097006022, 1997.
658
659 Yang, Q., Mayewski, P. A., Linder, E., Whitlow, S., and Twickler, M.: Chemical species spatial
660 distribution and relationship to elevation and snow accumulation rate over the Greenland Ice Sheet, *J*
661 *Geophys Res-Atmos*, 101, 18629-18637, 10.1029/96jd01061, 1996.
662
663
664

Sample	Volume (mm ³) ^a						Volume Fraction ^{a, b}			CsCl Mass Fraction ^{a, c}			
	Initial solution volume (μL)	Total CsCl mass (μg)	Gas	Water ice	LLR 2-10%	LLR >10%	Gas	Water ice	LLR 2-10%	LLR >10%	Water ice	LLR 2-10%	LLR >10%
<u>MillQ water</u>													
Freezer	500	0	5.96	430	0	0	0.014	0.986	0	0	--	--	--
Freezer, degassed	500	0	3.23	432	0	0	0.007	0.993	0	0	--	--	--
<u>1 mM CsCl</u>													
Freezer	750	126.3	5.07	716	2.35	0.141	0.007	0.990	0.003	0.00019	0.651	0.233	0.116
Freeze chamber	500	84.2	5.55	473	2.67	0.0176	0.012	0.983	0.006	0.000037	0.640	0.346	0.014
Liquid nitrogen	750	126.3	0	725	1.50	0	0	0.998	0.002	0	0.879	0.121	0.000

665
666 Table 1. Sample volumes and fractions by material type.
667

668 ^a “Gas” is defined as having a greyscale value of < 3996, “Water ice” is defined as containing < 2% liquid-like region (LLR), “LLR 2-10%” is
669 water ice containing an LLR fraction of between 2 and 10%, and “LLR > 10%” is water ice containing > 10% LLR. The original sample volume
670 (either 500 or 750 μL) is not fully captured in the volumes reported here. The segmentation process eliminates some of the lower part of the
671 sample, reducing the reported volume somewhat.

672 ^b Fraction of imaged sample volume (not initial solution volume). See text for details.

673 ^c Fraction of total CsCl mass present in each domain. Because the mass of CsCl present in the water ice compartment could not be determined
674 directly, we assumed any mass not present in either the LLR 2-10% or LLR >10% domain is present in the water ice domain.

675
676
677

678 **Figure Captions**

679
680 Figure 1. Radiodensity of pure water (red open squares, three data points) and of aqueous solutions
681 containing CsCl (blue triangles).
682

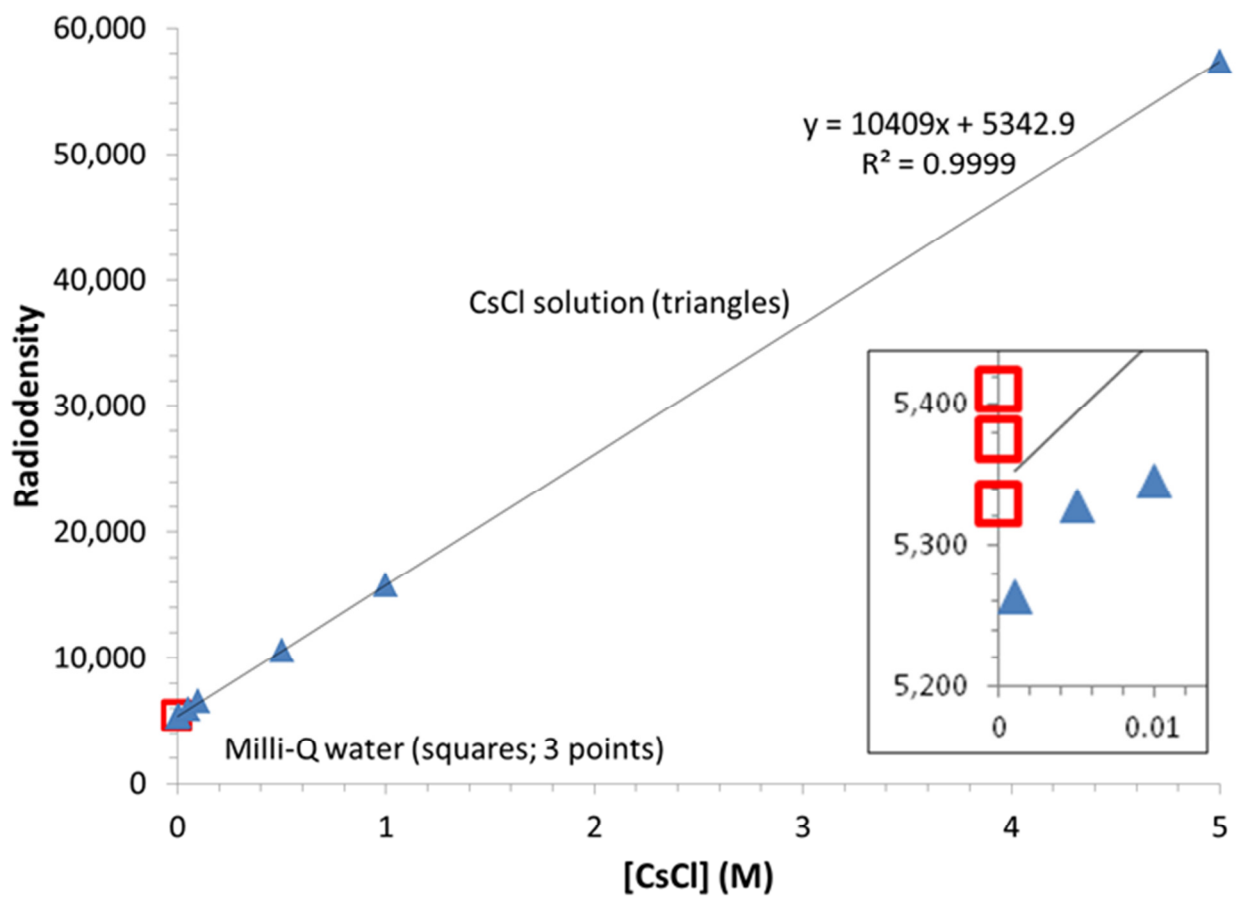
683 Figure 2. Reconstructed images (*a* and *b*) and histogram (*c*) of water ice samples frozen in a laboratory
684 freezer, imaged using microCT (~16 μm voxel size) and segmented to show air bubbles (light grey) and
685 the bulk ice matrix (darker grey). The glass sample vial is not shown. The ice in panel *a* was made using
686 air-saturated water, while that in *b* was made with water degassed with helium for 30 min before freezing.
687 Panel *c* shows the distributions of the radiodensities within the two samples, expressed as the fraction of
688 each voxel that would be occupied by a liquid-like region (LLR) assuming the total solute concentration
689 is determined by freezing point depression (i.e., 5.4 M at -10°C ; (Cho et al., 2002)).
690

691 Figure 3. Reconstructed images and histograms of ice samples frozen using three freezing methods and
692 with two different solutes. Samples were imaged using a ~16 μm voxel size and segmented to show air
693 bubbles (light grey), the bulk ice matrix (darker grey), voxels where $V_{\text{LLR}}/V_{\text{VOXEL}}$ is between 2 and 10%
694 (orange) and where $V_{\text{LLR}}/V_{\text{VOXEL}} > 10\%$ (red). The sample vial is not shown. a) 1.0 mM CsCl solution
695 frozen in freezer. b) magnification of the area in a) identified by the dashed red square. c) 1.0 mM CsCl
696 solution frozen in freeze chamber (without metal plates). d) magnification of the dashed-line area of c).
697 e) 1.0 mM CsCl solution frozen in liquid nitrogen. No air bubbles or inclusions are visible at this scale.
698 f) 1.0 mM Rose Bengal solution frozen in freeze chamber. g) histogram showing distribution of voxel
699 counts for the CsCl and Milli-Q water ice samples shown above: water ice frozen in freezer, black dotted
700 line; 1.0 mM CsCl frozen in LN2, orange line; 1.0 mM CsCl frozen in freezer, blue line; 1.0 mM CsCl,
701 frozen in freeze chamber, green line. The inset shows an expanded view from $V_{\text{LLR}}/V_{\text{VOXEL}} = -0.1$ to 0.1.
702

703 Figure 4. Side-by-side micro CT cross sections of the same sample (1.0 mM CsCl, frozen in laboratory
704 freezer) imaged at approximately 16 μm (panel a) and 2 μm (panel b) voxel sizes. Lighter tones indicate
705 areas of higher radiodensity, i.e., higher solute amounts. The scale bar applies to both images.
706

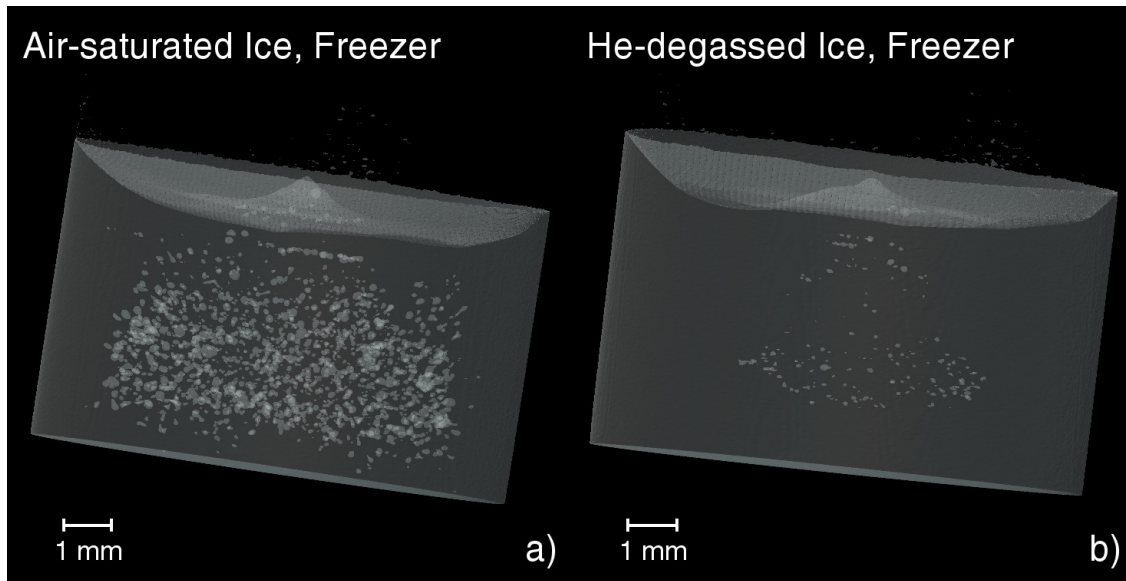
707 Figure 5. Vertically sliced X-ray images of a 1.0 mM CsCl ice (laboratory freezer, voxel resolution ~ 2
708 μm) after 0, 11, and 22 hours in the CT sample chamber. Lighter tones indicate areas of higher
709 radiodensity (e.g., greater CsCl amounts). Air bubbles are visible as darker gray spheres. The
710 temperature of the sample holder was set at -10°C , but the top of the sample was approximately 1.3°C
711 warmer than the bottom, corresponding to a temperature gradient of approximately $0.13^\circ\text{C mm}^{-1}$.
712 Arrows highlight two of the areas where CsCl moves along the direction of the temperature gradient,
713 from colder to warmer.
714

715 Figure 1
716

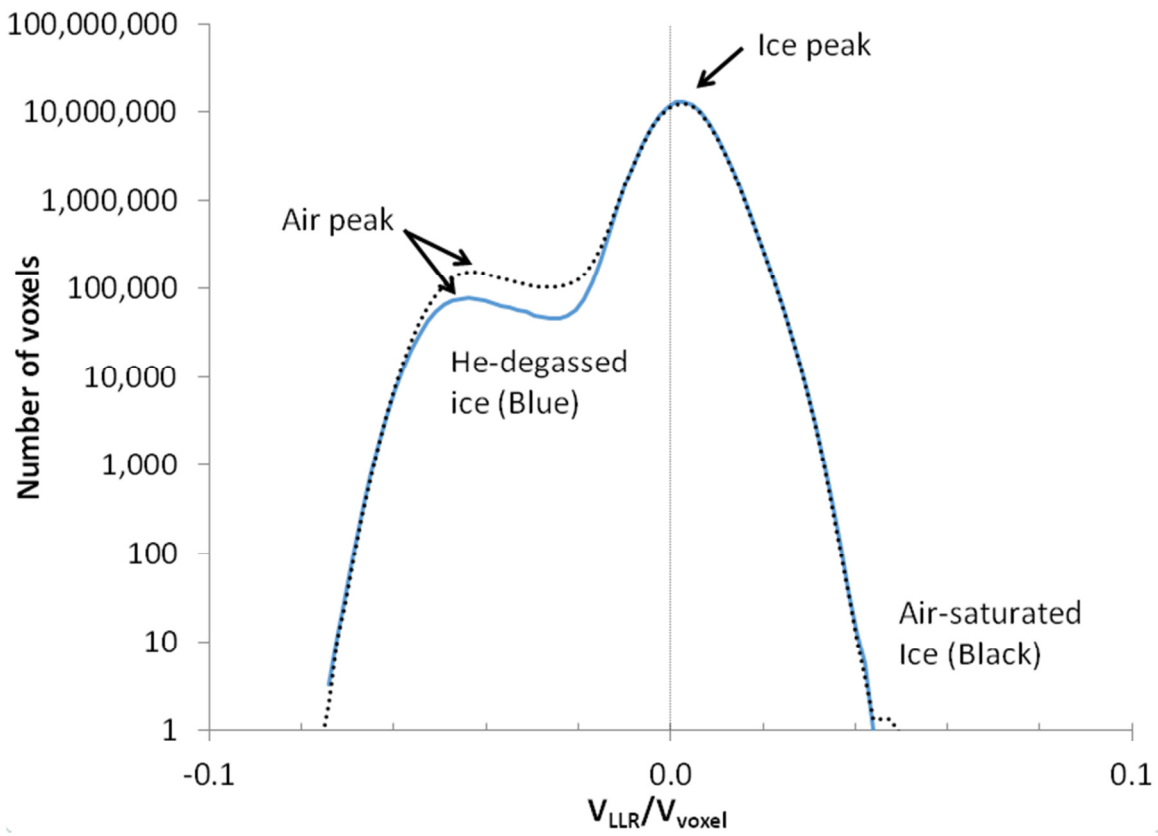


717
718

719 Figure 2
720

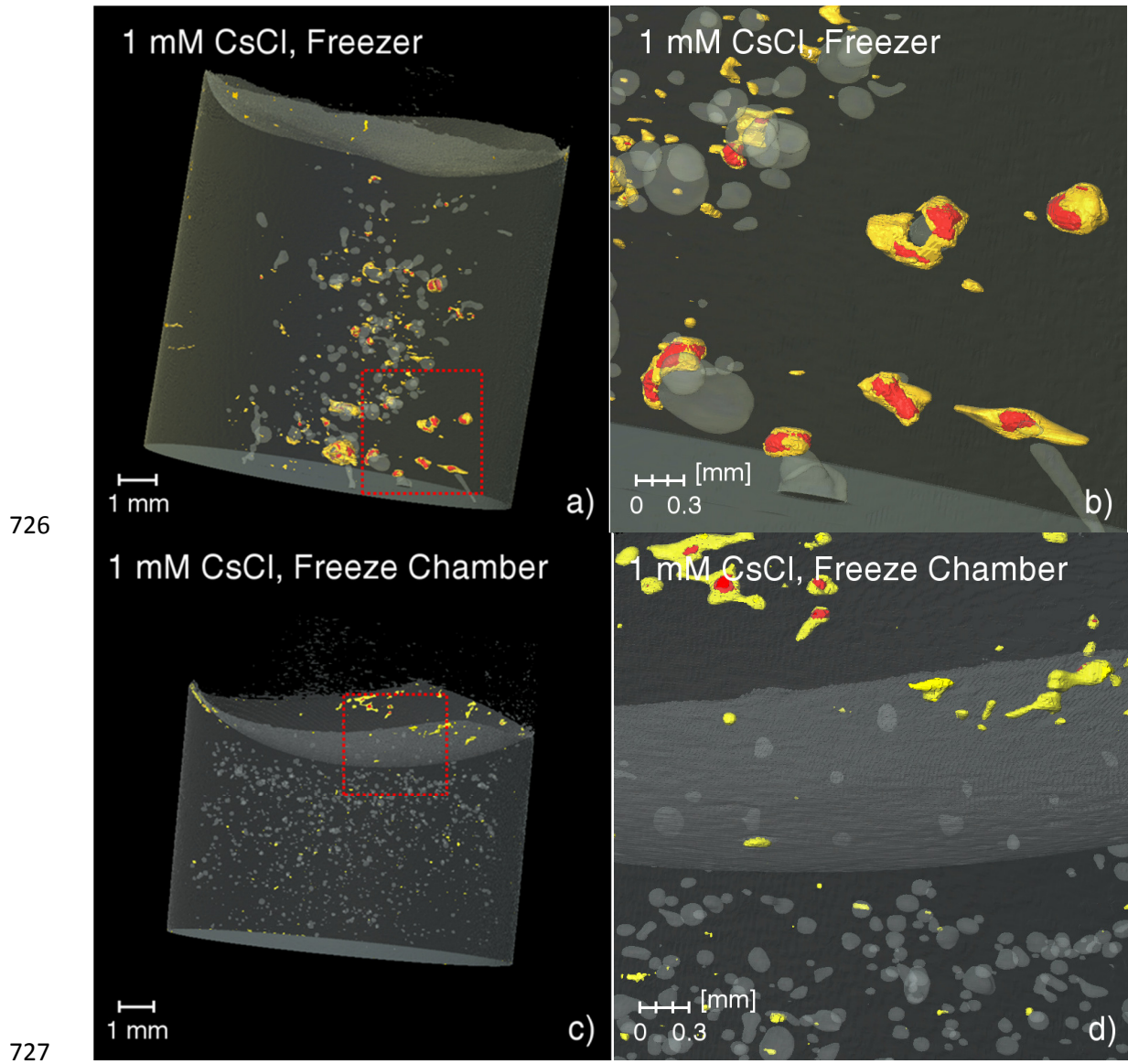


721



722
723

724 Figure 3
725

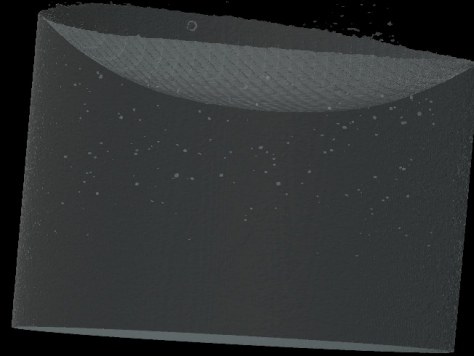


1 mM CsCl, LN2



1 mm

1 mM Rose Bengal, Freeze Chamber

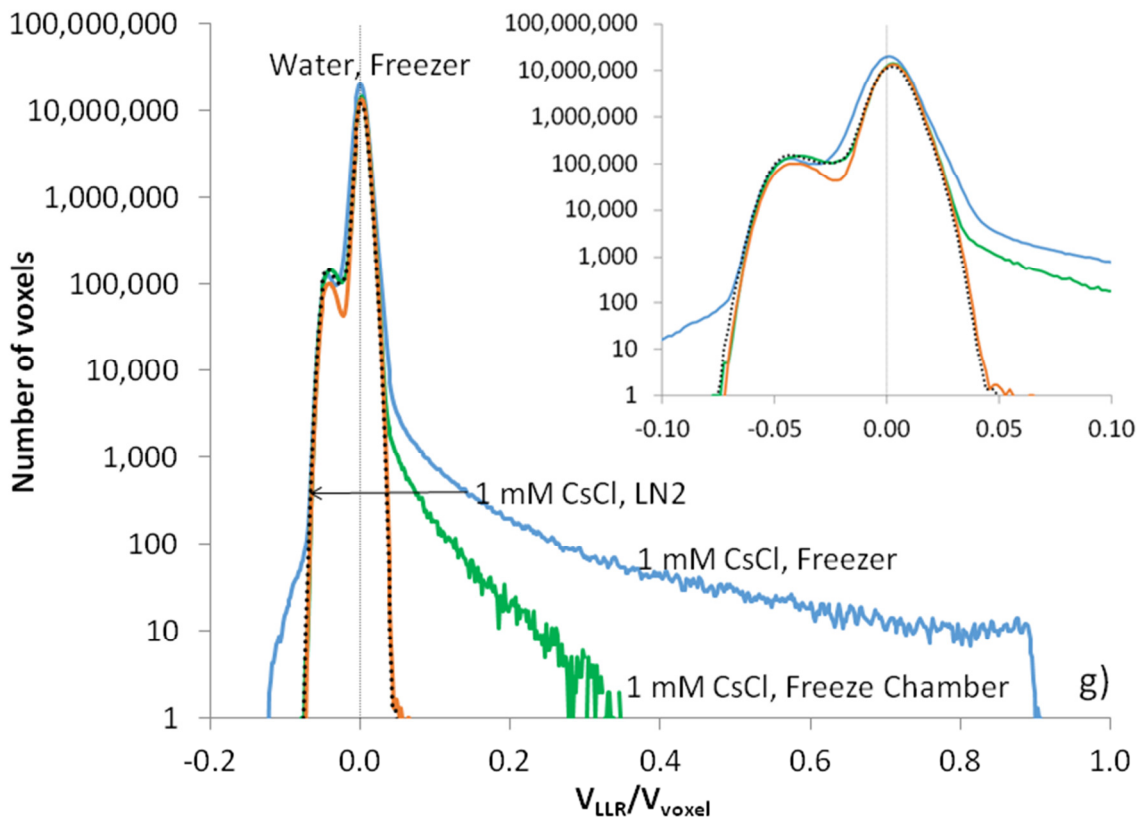


e)

1 mm

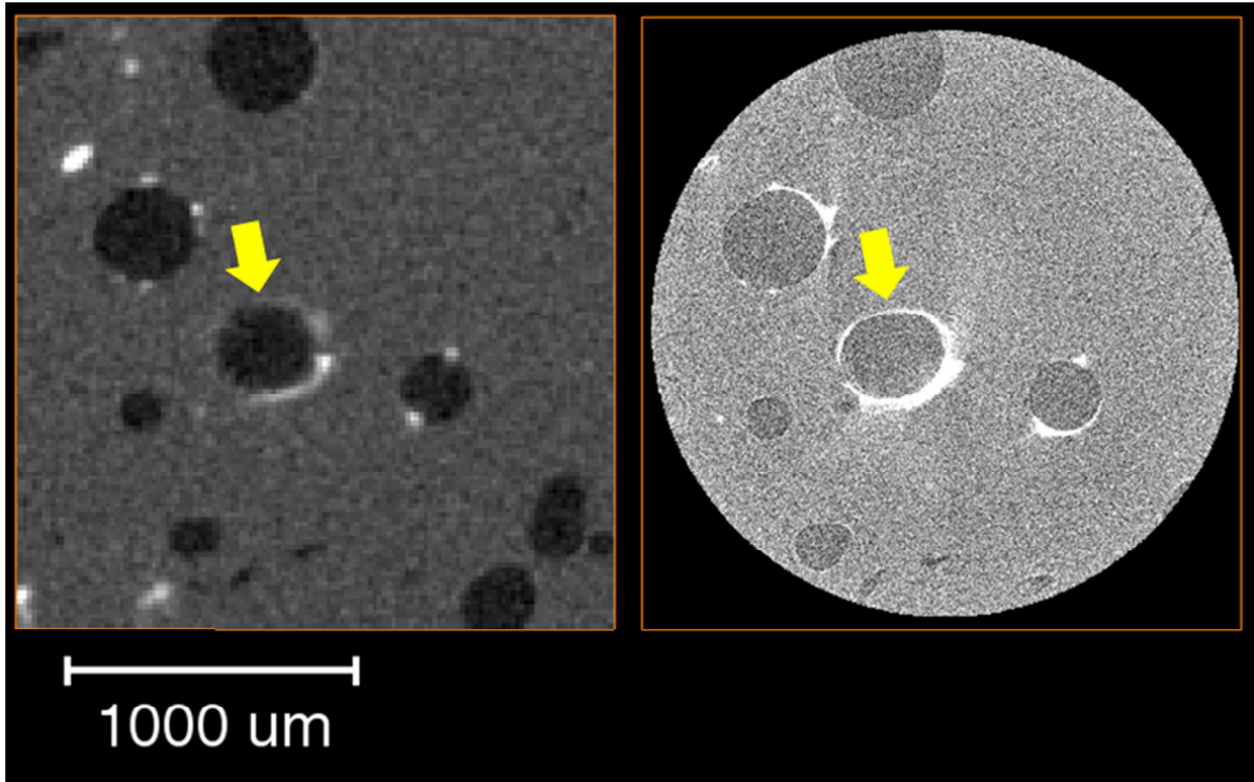
f)

728



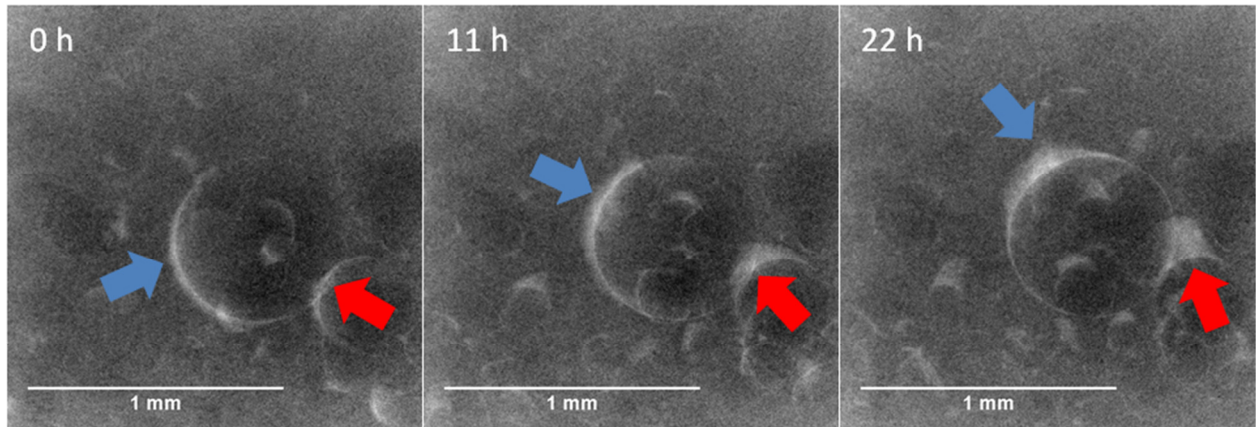
729
730

731 Figure 4
732



733
734

735 Figure 5
736



737